Contents lists available at ScienceDirect

Applied Catalysis B: Environmental

Fabrication and high photocatalytic performance of noble metal nanoparticles supported on 3DOM InVO$_4$–BiVO$_4$ for the visible-light-driven degradation of rhodamine B and methylene blue

Kemeng Ji [a], Jiguang Deng [a,*], Hongjun Zang [b], Jiuhui Han [c], Hamidreza Arandiyan [d], Hongxing Dai [a,*]

[a] Key Laboratory of Beijing on Regional Air Pollution Control, Beijing Key Laboratory for Green Catalysis and Separation, and Laboratory of Catalysis Chemistry and Nanoscience, Department of Chemistry and Chemical Engineering, College of Environmental and Energy Engineering, Beijing University of Technology, Beijing 100124, China
[b] School of Environmental and Chemical Engineering, Tianjin Polytechnic University, Tianjin 300387, China
[c] World Premier International (WPI) Research Center, Advanced Institute for Materials Research, Tohoku University, Sendai 980-8577, Japan
[d] Particles and Catalysis Research Group, School of Chemical Engineering, The University of New South Wales, Sydney, NSW 2052, Australia

ABSTRACT

Three-dimensionally ordered macroporous (3DOM) InVO$_4$–BiVO$_4$ (InBi-3D) and its supported noble metal M nanoparticles (xM/InBi-3D; x = 0.08–0.13 wt%; M = Au, Ag, Pd, Pt) were prepared using the polymethyl methacrylate-templating and polyvinyl alcohol- or polyvinyl pyrrolidone-assisted reduction methods, respectively. Physical properties of the materials were characterized by a number of analytical techniques. Photocatalytic activities of the xM/InBi-3D samples were evaluated for the degradation of rhodamine B (RhB), methylene blue (MB), and their mixture. It is found that the as-fabricated samples possessed a surface area of 17–30 m^2/g, a M particle size of 2.5–3.8 nm, and a bandgap energy of 2.50–2.56 eV. The xM/InBi-3D photocatalysts showed high activities for the degradation of RhB, MB, and RhB + MB in the presence of a small amount of H$_2$O$_2$ under visible-light irradiation, among which complete degradation of RhB, MB, and RhB + MB was achieved within 50, 90, and 120 min over 0.08 wt% Au/InBi-3D, respectively. The degradation of MB and RhB fellow the zero- and first-order reaction mechanisms with respect to dye concentration, respectively. It is concluded that the high photocatalytic efficiency of the Au-loaded sample in the removal of organic dyes was associated with its high surface area, high-quality 3DOM hierarchical architecture, InVO$_4$–BiVO$_4$ composite, and high dispersion of gold nanoparticles.

© 2014 Elsevier B.V. All rights reserved.

1. Introduction

Since the interests in harvesting and conversion of solar energy revive promptly in recent years, photocatalysis technology, which can directly convert solar energy into chemical energy, has received much attention [1]. Development of semiconductor materials is the focus in heterogeneous photocatalysis. Over a semiconductor photocatalyst, photons generated under UV or visible light irradiation are first absorbed to yield high-energy charge carriers (electron (e$^-$)/hole (h$^+$) pairs), and then these charge carriers are separated from each other and diffuse to catalytically active sites at the semiconductor–liquid interfaces to drive chemical transformation [1]. Generally speaking, an efficient semiconductor photocatalyst needs an appropriate electronic structure, an active site distribution, and a suitable geometry, so that it can provide adequate absorption of sunlight, effective conversion of photons into e$^-$/h$^+$ pairs, and expedient separation of the generated charge carriers [1,2]. Therefore, fabricating a photocatalyst that meets the above requirements is full of challenge.

To achieve this goal, one choice is to obtain hierarchical three-dimensional nanostructures, because they can provide large surface areas (abundant active sites), narrow-distributed nanoparticles (short charge-carrier transport paths), favorable optical configurations, and good pore interconnectivity (enhanced light harvesting) [3,4]. The other choice is to tailor-make the bandgap energies of materials by doping with various transition metal or non-metal atoms so that their optical responses can be extended to the visible or near infrared light regions [5]. Noble metal (e.g., Au, Ag, Pd, and Pt) nanoparticles exhibit characteristic optical and physical properties (relative high absorption coefficients for

* Corresponding authors. Tel.: +86 10 6739 6118; fax: +86 10 6739 1983.
E-mail addresses: jgdeng@bjut.edu.cn (J. Deng), hxdai@bjut.edu.cn (H. Dai).

photons and resistance against self degradation) [1,4–6]. Strong evidence reveals that the plasmonic effect not only plays a quite positive role in enhancing the rate of photocatalytic reactions on nearby semiconductors, but also possibly interacts with the entire solar spectrum when appropriate resonant wavelength and SPR intensity are obtained in a well-designed plasmonic nanostructure [1]. It has been reported that metal/semiconductor composite materials, such as Au/TiO_2 or $Ag/N-TiO_2$ composites [1], Ag@AgCl cubic cages with well-defined hollow interiors [4], hybrid nanoparticles with cubic AgCl cores and Ag nanograin coating [5], Ag nanoparticles/AgX (X = Cl, Br, and I) [6], $Ag_3VO_4/AgBr/Ag$ ternary hybrids [7], showed significantly higher photocatalytic degradation rates than their single counterparts in a number of reactions [1]. Although much improved photocatalytic activities could be achieved over these metal/semiconductor composite materials, they still lacked the aforementioned optimized architecture.

In recent years, three-dimensionally ordered macroporous (3DOM) perovskite-type oxides [8–10] and transition-metal oxides [11–13] have been reported in the literature. The 3DOM architecture is a replicated shell structure of a face-centered-cubic opal based on self-assembly of uniform monodispersed polymer microspheres, which offers relatively large surface areas and high porosity (74% void volume) [14]. Such a hierarchically porous system with secondary pore channels in an interconnected morphology is beneficial for the availability of internal surface, accessibility of more amount of open pores, and diffusivity of reactants and products [15,16]. The ordered nanostructures in TiO_2 [14,16–18] and $BiVO_4$ [19] as well as other wide bandgap semiconductor materials [17] have been realized to be important in photocatalysis. The periodical three-dimensional inverse opal structure is not only conducive to electron transport and light trapping due to the increased optical path length by multi-scattering, but also can provide an additional photonic bandgap effect to facilitate the light–matter interaction by controlling the propagation of light via the modes of back reflections, slow photons, and surface resonance [14].

Previously, we reported that 3DOM $InVO_4$ exhibited much better photocatalytic performance for methylene blue (MB, $C_{16}H_{18}N_3SCl$) degradation than the bulk $InVO_4$ [20], indicating that a 3DOM structure was beneficial for improvement in activity. However, 3DOM $InVO_4$ showed poor photocatalytic performance for rhodamine B (RhB, $C_{28}H_{31}ClN_2O_3$) degradation, even when 15 wt% CoO_x was loaded on 3DOM $InVO_4$ its photocatalytic performance was still not satisfactory [21]. It is well known that $BiVO_4$ can effectively photocatalyze the degradation of RhB. Inspired by the above considerations as well as some previous works on $InVO_4$ [20,21] and $BiVO_4$ [22,23] in our group, we herein report the fabrication of 3DOM $InVO_4$–$BiVO_4$ (denoted as InBi-3D) and its supported noble metal M (xM/InBi-3D; x = 0.08–0.13 wt%; M = Au, Ag, Pd, Pt) nanoparticles via the polymethyl methacrylate (PMMA)-templating and polyvinyl alcohol (PVA)- or polyvinyl pyrrolidone (PVP)-assisted reduction routes, respectively. We envision that the composite created by introduction of a small amount of $BiVO_4$ in less active $InVO_4$ would be beneficial for the enhancement of carrier transfer in the materials. In the meanwhile, loading a trace amount of nanoscale noble metals could undoubtedly enable the 3DOM architecture to capture and transform light energy more effectively due to their plasmonic behaviors. As important industrial dyes that are resistant to biodegradation and direct photolysis, MB or RhB is the most used model pollutant [24–27]. Hence, we evaluate photocatalytic activities of xM/InBi-3D for the degradation of RhB, MB and RhB + MB. A possible reaction mechanism for the photodegradation of mixed dyes over 0.08 wt% Au/InBi-3D was proposed.

2. Experimental

2.1. Photocatalyst fabrication

The InBi-3D support was fabricated using the ascorbic acid-assisted PMMA-templating strategy. The well-arrayed PMMA microspheres (ca. 300 nm in average diameter) were synthesized according to the procedures described elsewhere [12]. In a typical fabrication, 8.0 mmol of $In(NO_3)_3 \cdot 4.5H_2O$, 2.0 mmol of $Bi(NO_3)_3 \cdot 5H_2O$, and 10.0 mmol of ascorbic acid were first dissolved in a mixed solution of ethylene glycol (1.5 mL), methanol (7.5 mL), nitric acid (1.0 mL, 68 wt%), and deionized water (7.0 mL) to obtain a colored transparent solution at 70 °C, and then 10.0 mmol of NH_4VO_3 was added into the above mixture. After complete dissolution, the as-obtained solution was first cooled to room temperature (RT), and then 3.0 g of the PMMA microsphere template was soaked into the mixed solution for 3 h. After being filtered and dried adequately, the sample was first treated in a N_2 flow (100 mL/min) at a ramp of 1 °C/min from RT to 300 °C and maintained at this temperature for 3 h, and then calcined in an air flow (100 mL/min) at a ramp of 1 °C/min from 300 to 450 °C and kept at 450 °C for 4 h, thus obtaining the InBi-3D sample with an $InVO_4/BiVO_4$ molar ratio of 4/1. For comparison purposes, we also adopted a hydrothermal method to fabricate referenced $InVO_4$–$BiVO_4$ (denoted as InBi-ref): 1.972 g of triblock copolymer Pluronic P123 ($M_{av.}$ = 5800) and 0.004 mol of glucose were added to the above mixed aqueous solution containing $In(NO_3)_3 \cdot 4.5H_2O$, $Bi(NO_3)_3 \cdot 5H_2O$, and NH_4VO_3, 80 mL of the obtained mixture (pH ca. 2.0) was transferred into a 100-mL Teflon-lined stainless steel autoclave for hydrothermal treatment at 180 °C for 6 h. The as-obtained solid was fully washed, dried, and at last calcined in air at a ramp of 1 °C/min from RT to 500 °C and maintained at this temperature for 3 h, thus obtaining the InBi-ref sample.

The xM/InBi-3D (x = 0.08–0.13 wt%; M = Au, Ag, Pd, Pt) photocatalysts were prepared via a PVA- or PVP-protected reduction route. The noble metal aqueous solution (0.01 mol/L) was in advance prepared with $HAuCl_4$, $AgNO_3$, $PdCl_2$, and H_2PtCl_6 as metal source in the presence of PVA (M = Au, Ag, Pd, and Pt; M/PVA mass ratio = 1.5/1) or PVP (Ag/PVP monomer mass ratio = 1/1.5), respectively. The typical preparation procedure is as follows: (i) A stoichiometric amount of the M-containing solution was first diluted with deionized water to be 1/50 in concentration; (ii) an $NaBH_4$ aqueous solution (0.05 mol/L) was rapidly injected into the above solution (M/$NaBH_4$ molar ratio = 1/5) in ice-water bath under vigorous N_2-bubbling for 20 min, obtaining a sol; (iii) a desired amount of InBi-3D was added to the sol (theoretical M loading = 0.15 wt%), and the mixture was agitated via N_2 bubbling for 10 h; and (iv) the obtained sample was filtered, dried at 200 °C for 2 h, washed with deionized water, and further dried at 80 °C for 10 h.

2.2. Photocatalyst characterization

Elemental analysis of the samples was carried out on a X-ray fluorescence (XRF) spectrometer (Magix PW2403) and an inductively coupled plasma atomic emission spectroscopic (ICP-AES, Thermo Electron IRIS Intrepid ER/S) apparatus. X-ray powder diffraction (XRD) patterns of the samples were collected on a Bruker D8 Advance diffractometer equipped with Cu Kα radiation and Ni filter (λ = 0.15406 nm), and the operating voltage and current were 40 kV and 35 mA, respectively. Laser Raman spectra of the samples were acquired using a Renishaw inVia Raman microscope with an excitation laser wavelength of 785 nm. Scanning electron microscopic (SEM) images and chemical compositions of the samples were measured using a Gemini Zeiss Supra 55 apparatus (operating

voltage = 5 kV) equipped with an X-ray energy-dispersive spectroscopy (EDS). Transmission electron microscopic (TEM) images and selected-area electron diffraction (SAED) patterns of the samples were recorded on a JEOL-2010 equipment operated at 200 kV. Surface areas and pore-size distributions of the samples were calculated using the Brunauer–Emmett–Teller (BET) and Barrett–Joyner–Halenda (BJH) methods, respectively, according to the nitrogen adsorption–desorption isotherms measured at −196 °C on a Micromeritics ASAP 2020 analyzer, in which the samples were degassed at 200 °C for 2 h. The ultraviolet–visible (UV–vis) diffuse absorbance and reflectance spectra of the samples in the range of 200–900 nm were determined on a Shimadzu UV-2450 spectrophotometer using $BaSO_4$ as the standard. X-ray photoelectron spectroscopic (XPS) technique was used to measure the metal oxidation states and surface element compositions of the samples on a Thermo Scientific K-Alpha, with the excitation source and resolution being Al Kα (1486.67 eV) and 0.1 eV, respectively. Binding energies (BEs) of In 3d, Bi 4f, V 2p, O 1s, and C 1s were calibrated against the C 1s signal at BE = 284.6 eV. Fourier transform infrared (FT-IR) spectra of the samples were recorded in the 400–4000 cm^{-1} range on a Bruker Vertex 70 spectrometer, with KBr as the dispersion medium.

### 2.3. Photocatalytic evaluation

Photocatalytic degradation of RhB (initial concentration $C_0 = 15$ mg/L), MB ($C_0 = 20$ mg/L) or RhB ($C_0 = 15$ mg/L) + MB ($C_0 = 20$ mg/L) aqueous solution over the InBi-based and Degussa P25 (TiO_2) samples was carried out in a quartz reactor (QO250, Beijing Changtuo Sci. & Technol. Co., Ltd.) under visible-light irradiation (300-W Xe lamp (PLS-SXE300, Tianjin Dongli Teaching Instrument Factory) and a 400-nm cutoff filter). Prior to irradiation, the suspension (0.1 g of the sample in 100 mL of the dye aqueous solution containing 0.6 mL of H_2O_2 aqueous solution (30 wt%)) was ultrasonicated for 0.5 h, and then magnetically stirred for 3 h in the dark to ensure the establishment of adsorption–desorption equilibrium in the reaction system. During the irradiation, 5 mL of the suspension was sampled at a regular interval. The reactant solution was kept at RT by flowing cool water. After the photocatalyst in the suspension was removed through centrifugation, the absorption spectra of the remaining solutions were recorded on the aforementioned UV–vis equipment. Photocatalytic degradation over each sample was evaluated by the temporal concentration (C_t) of RhB, MB or RhB + MB, which was determined in terms of their standard concentration versus absorbance curves and the changes in intensity of the absorbance at the corresponding absorption band maximum of RhB (554 nm) or MB (665 nm).

3. Results and discussion

3.1. Crystal phase structure

The M (M = Au, Ag, Pd, and Pt) compositions of the samples were determined by the ICP-AES technique, and the results are summarized in Table 1. It is observed that the M loading in the samples was 0.08, 0.11, 0.10, and 0.13 wt% for Au, Ag, Pd, and Pt, respectively, lower than their theoretical values (0.15 wt%). The discrepancy in real and theoretical M loadings was due to the washing and filtering operations during the photocatalyst preparation processes. Fig. 1A shows the XRD patterns of the samples. Because of the low M loadings, the diffraction peaks attributable to the M phases did not appear. From Fig. 1A, one can clearly see that the InBi-ref sample contained two main phases: orthorhombic InVO$_4$ (JCPDS PDF# 48-0898) and monoclinic BiVO$_4$ (JCPDS PDF# 14-0688); in the other 3DOM-structured samples, however, besides of a small
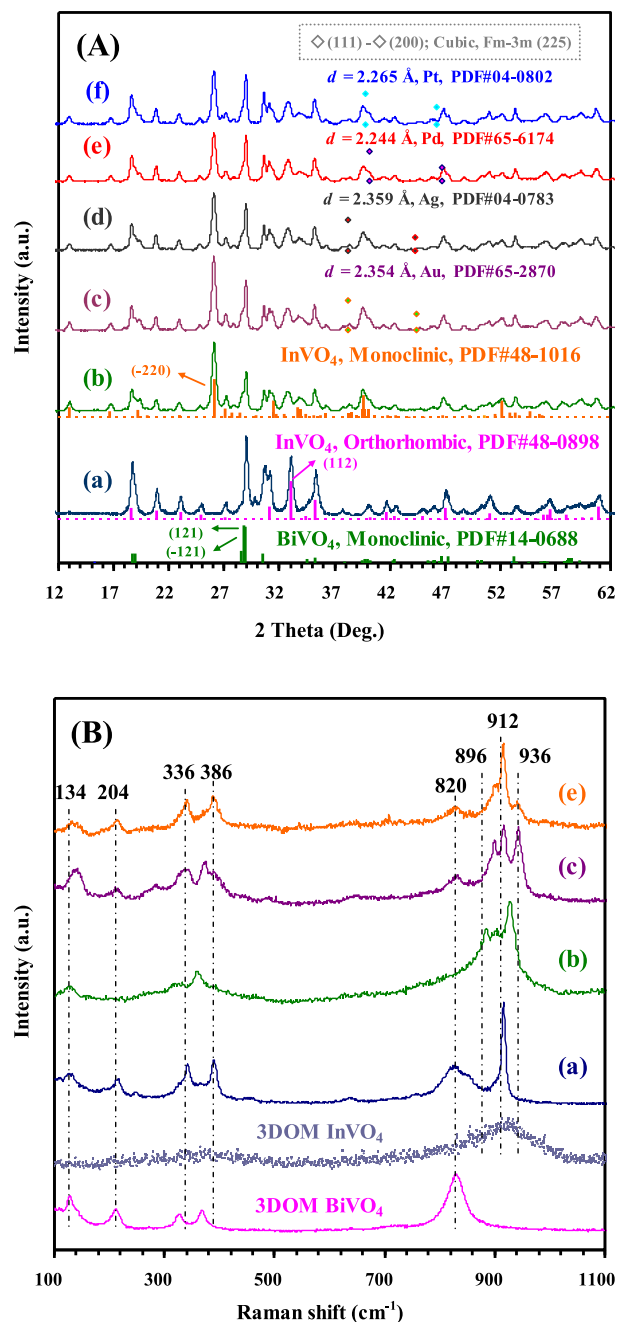
Fig. 1. (A) XRD patterns, (B) Laser Raman spectra, (C) nitrogen adsorption–desorption isotherms, and plots of $(\alpha h\nu)^2$ versus $h\nu$ as well as UV–vis diffuse reflectance spectra (inset of (D)) of (a) InBi-ref, (b) InBi-3D, (c) Au/InBi-3D, (d) Ag/InBi-3D, (e) Pd/InBi-3D, and (f) Pt/InBi-3D.

amount of orthorhombic InVO$_4$, there was presence of monoclinic InVO$_4$ (JCPDS PDF# 48-1016) and monoclinic BiVO$_4$, and both constituted the main framework of the InBi-3D support. These results indicate that the InVO$_4$–BiVO$_4$ composite was formed in each of the xM/InBi-3D samples, which might be superior in enhancing the photocatalytic performance to that in Ag$_3$VO$_4$/AgBr generated via the simple loading route [7].

As can be seen from Table 1, the calculated grain sizes of the samples were 18.9–20.3 nm for InVO$_4$ and 19.6–23.4 nm for BiVO$_4$, indicating that all of the samples had a narrow grain size distribution. Fig. 1B shows the Raman spectra of the Au/InBi-3D, Pd/InBi-3D, and InBi-3D samples. Apparently, the five characteristic Raman peaks associated with monoclinic BiVO$_4$ at ca. 134

Table 1
The real M loadings, M and InVO$_4$–BiVO$_4$ particles sizes, BET surface areas, pore volumes, and bandgap energies of the as-fabricated samples.

| Sample	M loading (wt%) [a]	Particle size (nm)		Surface area (m^2/g)/pore volume (cm^3/g)			Bandgap energy (eV)
		M [b]	InVO$_4$–BiVO$_4$ [c]	Macropore	Mesopore	Total	
InBi-ref	0.0	–	19.7	0.8/0.016	12.5/0.022	13.3/0.037	2.53
InBi-3D	0.0	–	19.6	4.9/0.143	25.8/0.027	30.7/0.170	2.56
0.08 wt% Au/InBi-3D	0.08	3.81	22.3	13.0/0.221	12.5/0.032	25.1/0.253	2.54
0.11 wt% Ag/InBi-3D	0.11	3.23	22.3	12.0/0.234	11.7/0.025	24.1/0.259	2.53
0.10 wt% Pd/InBi-3D	0.10	3.85	22.8	5.7/0.112	22.2/0.112	27.9/0.224	2.50
0.13 wt% Pt/InBi-3D	0.13	2.58	23.4	5.0/0.130	12.0/0.016	17.0/0.145	2.54

[a] Determined by the ICP-AES technique.
[b] Estimated according to the TEM images.
[c] Data calculated based on the XRD results according to the Scherrer equation using the FWHM of the (1 2 1) line of InVO$_4$–BiVO$_4$.

and 204 cm^{-1} (the rotation/translation modes of BiVO$_4$), 336 and 386 cm^{-1} (the asymmetric and symmetric deformation modes of VO$_4^{3-}$ tetrahedron), and 820 cm^{-1} (the stretching mode of V–O bonds) increased in intensity after the loading of M [23]. The three bands at 869, 912, and 936 cm^{-1} could be attributed to the stretching mode of V–O bonds in InVO$_4$. There was a shift and change in intensity of these bands after the loading of M, indicating an alteration in metal – oxygen bond in the local structure [23]. However, the InBi-ref sample displayed two strong Raman bands at 820 and 912 cm^{-1}, in good agreement with its crystal phase compositions (BiVO$_4$ and InVO$_4$) reflected from the XRD pattern.

3.2. Morphology, pore structure, surface area, and light absorption property

Morphologies of the InBi-3D and *x*M/InBi-3D samples were investigated by the SEM and TEM techniques, and their representative images are shown in Figs. 2 and 3, respectively. The InBi-ref sample contained a number of porous microspherical entities and a small amount of microcubes (Fig. S1). A well-defined 3DOM structure was observed in the InBi-3D sample (Fig. 2a), the macropore sizes, window sizes (diameters of pores between neighboring

macropores), and wall thicknesses were in the ranges of 100–200, 50–90, and 20–40 nm (Fig. 2b–f), respectively. It has been reported that in a photocatalytic reaction, macropores could facilitate the migration of surface charges but impede the migration of bulk charges, while small windows were beneficial for the migration of charges both in the bulk and on the surface [19]. From Fig. 2c–f, one can see a number of nanovoids randomly distributed on the macropore skeletons, which were similar to 3DOM InVO$_4$ [20,21]. These nanovoids could play a significant role in improving surface area, reactant adsorption, and light harvesting of the sample [28]. The lattice spacings (*d* value) were ca. 0.338 and 0.531 nm (Fig. 2g and h), rather close to those of the (−2 2 0) and (−1 1 1) planes of monoclinic InVO$_4$ (JCPDS PDF# 48-1016). No lattice spacings assignable to the crystal planes of BiVO$_4$ (JCPDS PDF# 14-0688) were recorded. That is to say, BiVO$_4$ might possess a poor crystallinity, and it was mixed together with InVO$_4$ to make up of the walls of the 3DOM framework, in line with the EDS result (inset of Fig. 2b and Table 2). Fig. 3 illustrates the local microstructures of the *x*M/InBi-3D samples. The M nanoparticles were well dispersed on the macroporous skeletons of InBi-3D (Fig. 3a–d). The *x*M/InBi-3D samples displayed a narrow M particle size distribution, and the average diameters of Au, Ag, Pd, and Pt nanoparticles were 3.81, 3.23, 3.85, and 2.58 nm (Fig. S2), respectively. More details can be seen from their TEM
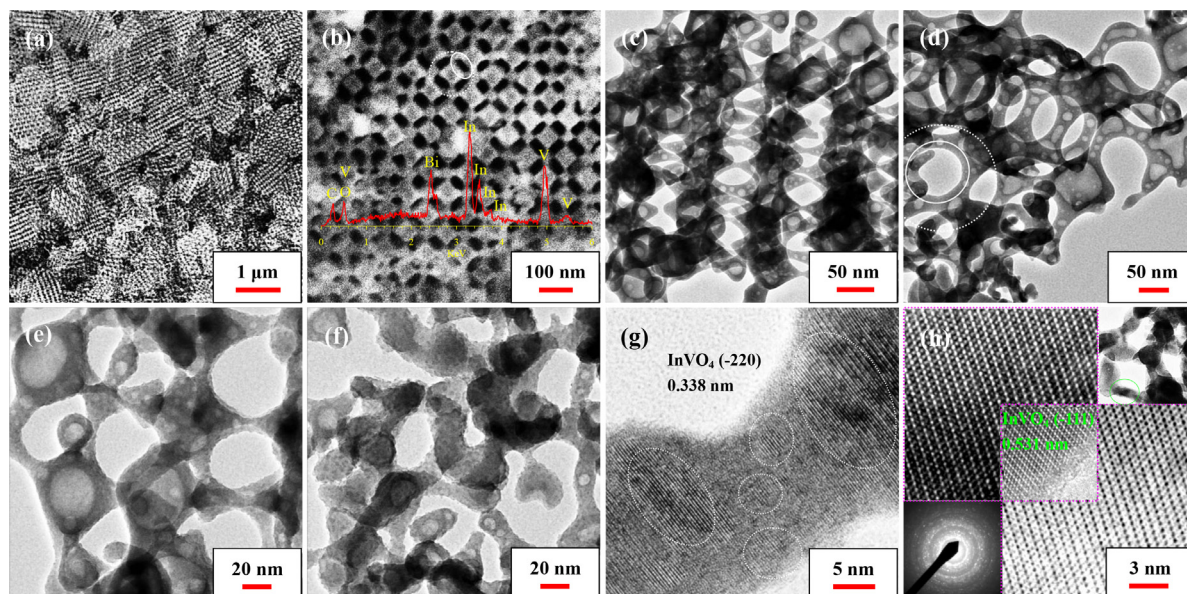
Fig. 2. (a, b) SEM and (c–h) TEM images as well as the SAED pattern (inset) of the InBi-3D sample.
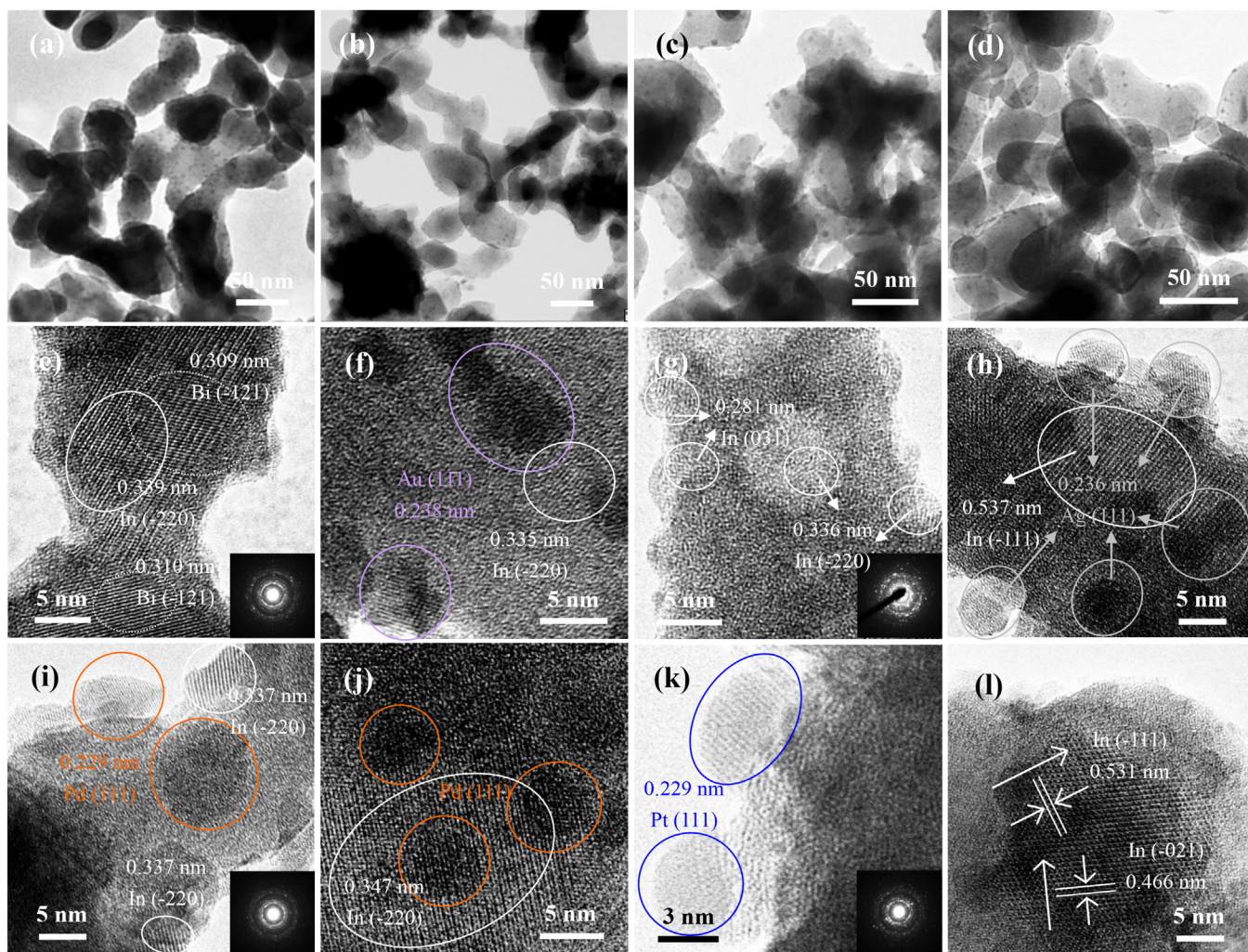
Fig. 3. TEM images and the SAED patterns (insets) of M/InBi-3D (M = Au (a, e, f), Ag (b, g, h), Pd (c, i, j), and Pt (d, k, l)).

images (Fig. 3e–l). Although the xM/InBi-3D samples were treated at 200 °C for 2 h, they still exhibited weak crystallinity, which could also be reflected from their inset SAED patterns. Multiple crystal planes ((−2 2 0) in Fig. 3e–g, i and j, (0 3 1) in Fig. 3g, (−1 1 1) in Fig. 3h and l, and (−0 2 1) in Fig. 3g) attributable to monoclinic InVO$_4$ were exposed on the skeletons. No significant exposed planes of BiVO$_4$ were observed, except for the (−1 2 1) plane ($d \approx 0.310$ nm) in Fig. 3e, but it might also correspond to the (−3 1 1) plane of InVO$_4$. This result confirms that BiVO$_4$ was poor in crystallinity. Meanwhile, one can easily distinguish the M nanoparticles of xM/InBi-3D from their TEM images (Fig. 3f and h–k). Furthermore, the original nanovoids on the skeletons (Fig. 3g) can also be seen after the loading of M.

Fig. 4A shows the N$_2$ adsorption–desorption isotherms and pore-size distributions of the samples. Each of the samples displayed a type II isotherm and a type H3 hysteresis loop in the relative pressure range of 0.9–1.0, indicative of macropore presence. Such a deduction was substantiated by the inset pore-size distributions. Some nanovoids or mesopores were present in the macroporous structure, and they contributed a lot to the BET surface areas of the samples (Table 1). Compared to the InBi-3D sample (surface area = 30.7 m^2/g and pore volume = 0.170 cm^3/g), the xM/InBi-3D samples (except Pt/InBi-3D) showed a slightly lower surface area (24.1–27.9 m^2/g) and much larger pore volume (0.224–0.259 m^3/g), which were much higher than those (13.3 m^2/g and 0.037 cm^3/g) of the InBi-ref sample. The surface

areas of xM/InBi-3D were lower than those of 3DOM InVO$_4$ (35.1–52.3 m^2/g) [20], but higher than those of 3DOM BiVO$_4$ (18.1–23.6 m^2/g) [22]. At the same time, one can also notice that the InBi-3D-supported Au and Ag samples displayed higher macropore surface areas and pore volumes but lower mesopore surface areas and pore volumes than the InBi-3D-supported Pd and Pt samples.

Fig. 4B illustrates the plots of ($\alpha h v$)^2 versus $h v$ as well as the UV–vis spectra of the samples. In addition to the slight enhancement in visible-light (480–800 nm) intensity, the xM/InBi-3D samples displayed a similar light absorption, and the bandgap energies (E_g = 2.50–2.56 eV) obtained from the intercept of the plot of ($\alpha h v$)^2 versus $h v$ [20–23] were quite close (Table 1). The broad light absorption scopes and appropriate E_g values (close to 2.50–2.55 eV of 3DOM InVO$_4$ [20] or 3DOM BiVO$_4$ [22]) indicate the good ability to absorb UV and visible light [29,30].

3.3. Surface composition, metal oxidation states, and oxygen species

Surface chemical states of the samples were studied by means of the XPS technique. Although there were no significant XPS signals of the noble metals (Au 4f, Ag 3d, Pd 3d, and Pt 4f) due to their small contents in the xM/InBi-3D samples, the In 3d, Bi 4f, V 2p$_{3/2}$, and O 1s XPS spectra were recorded (Fig. 5). In addition to the In 3d$_{3/2}$ (at BE = 443.8 eV) and In 3d$_{5/2}$ (at BE = 451.3 eV) peaks (Fig. 5A), there

Table 2
Binding energies and surface element compositions of the samples.

Sample	In 3d (eV)		Bi 4f (eV)		In/Bi molar ratio [a]	(In + Bi)/V molar ratio	Bi/V molar ratio	V 2p$_{3/2}$ (eV)		V^{4+}/V^{5+} molar ratio	O 1s (eV)		O$_{ads}$/O$_{latt}$ molar ratio
	3d$_{3/2}$	3d$_{5/2}$	4f$_{7/2}$	4f$_{5/2}$				V^{4+}	V^{5+}		O$_{latt}$	O$_{ads}$	
InBi-ref	443.9	451.0	158.6	163.8	4.75 (–)	1.94	0.34	514.8	516.4	0.29	529.7	532.3	2.39
InBi-3D	443.9	451.4	158.6	163.9	12.6 (5.51)	2.14	0.16	514.9	516.1	0.41	529.7	531.4	1.08
0.08 wt% Au/InBi-3D	443.9	451.5	158.7	164.0	6.25 (5.35)	1.16	0.16	–	516.8	0	530.5	531.7	0.60
0.11 wt% Ag/InBi-3D	443.9	451.2	158.7	164.0	5.74 (4.93)	1.52	0.23	–	516.5	0	529.6	531.7	3.29
0.10 wt% Pd/InBi-3D	443.8	451.4	158.7	163.9	6.70 (5.28)	1.25	0.16	–	516.9	0	530.5	531.7	0.93
0.13 wt% Pt/InBi-3D	443.8	451.4	158.6	164.1	6.60 (5.08)	1.63	0.21	–	516.0	0	530.4	531.6	0.85

[a] The data in parenthesis were determined by the EDS technique.
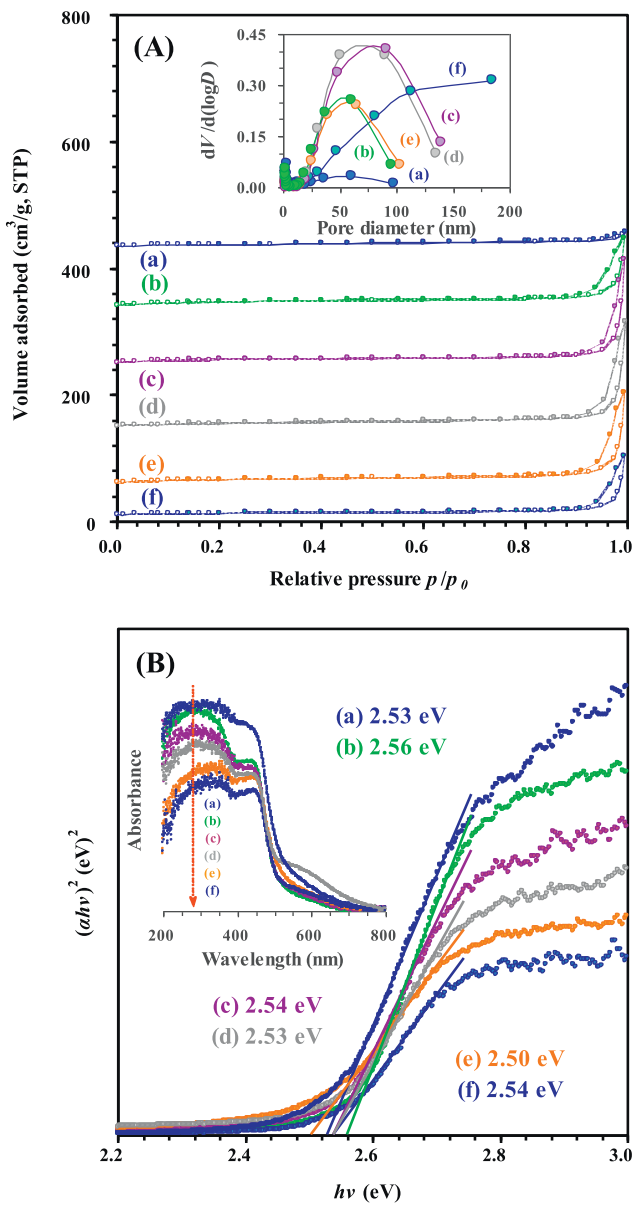
Fig. 4. (A) Nitrogen adsorption–desorption isotherms and (B) plots of $(\alpha h\nu)^2$ versus $h\nu$ as well as UV–vis diffuse reflectance spectra (inset) of (a) InBi-ref, (b) InBi-3D, (c) Au/InBi-3D, (d) Ag/InBi-3D, (e) Pd/InBi-3D, and (f) Pt/InBi-3D.

were still one or two shoulder(s) attributable to the surface In^{3+} species [20,21] in InVO$_4$ on the InBi-ref, InBi-3D, Ag/InBi-3D, and Pt/InBi-3D samples. The two spin-orbit splitting peaks of Bi 4f$_{7/2}$ and 4f$_{5/2}$ at 158.6 and 163.9 eV (Fig. 5B) were characteristic of Bi^{3+} species in BiVO$_4$ [22]. In the V 2p$_{3/2}$ XPS spectra (Fig. 5C), there were three signals at BE = 518.9, 514.9, and 516.1–516.9 eV, assignable to the surface V^{3+}, V^{4+}, and V^{5+} species [20–22]. As for the O 1s XPS spectra, one can decompose each of the O 1s XPS spectra into two components at BE = 529.5–530.5 and 531.4–532.4 eV, attributable to the surface lattice oxygen (O$_{latt}$) and adsorbed oxygen (O$_{ads}$, e.g. O$^-$, O$_2{}^{2-}$ or O$_2{}^-$) [10], respectively; another small signal at BE = 533.5 eV was also observed on the InBi-3D and Ag/InBi-3D samples, which might derive from the residual carbonate species formed due to the combustion of partially carbonized PMMA or PVP. From the calculated surface element compositions of the samples (Table 2), one can realize that there was an enrichment of indium on the surface, and indium was reported to be able to lower the conduction band [31]. Unlike the case of InVO$_4$, the Bi/V molar
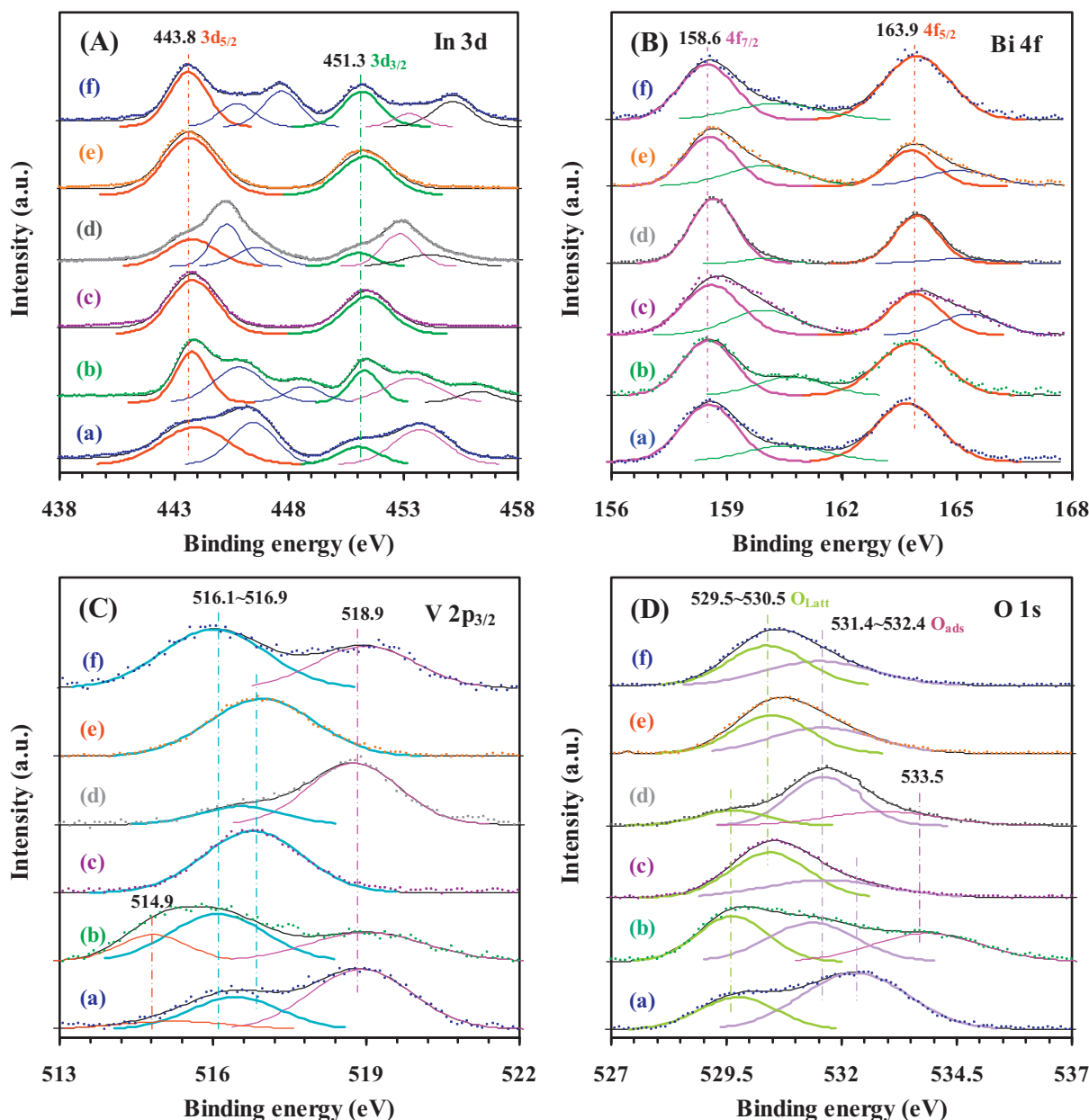
Fig. 5. (A) In 3d, (B) Bi 4f, (C) V 2p$_{3/2}$, and (D) O 1s XPS spectra of (a) InBi-ref, (b) InBi-3D, (c) Au/InBi-3D, (d) Ag/InBi-3D, (e) Pd/InBi-3D, and (f) Pt/InBi-3D.

ratios were close to the theoretical values, implying the formation of more homogeneous BiVO$_4$ phase. In the Au/InBi-3D and Pd/InBi-3D samples, either the Bi/V molar ratios (0.16) or (In + Bi)/V molar ratios (1.16 and 1.25) were not far away from their theoretical values, in good agreement with the recording of single XPS peak of each sample; the corresponding O$_{ads}$/O$_{latt}$ molar ratios (0.60 and 0.93) were the lowest. The InBi-ref sample showed a lower V^{4+}/V^{5+} molar ratio (0.29) but a higher O$_{ads}$/O$_{latt}$ molar ratio (2.39) than the InBi-3D sample (0.41 and 1.08, respectively). On the basis of the electroneutrality principle, a higher surface V^{4+}/V^{5+} molar ratio implies a higher amount of surface oxygen vacancies, thus giving a higher O$_{ads}$/O$_{latt}$ molar ratio because the O$_{ads}$ species are usually considered to mainly locate at the surface oxygen vacancies [32].

3.4. Photocatalytic performance and kinetic parameters

The degradation of RhB, MB, and MB + RhB aqueous solutions in the presence of a small amount (0.6 mL) of H$_2$O$_2$ were used to evaluate photocatalytic activities of the samples. Fig. 6A shows photocatalytic activities of the samples for RhB degradation under visible-light illumination. Usually, the dye concentration is proportional to its absorbance (Fig. S3). We monitored the concentration (C_t/C_0, C_0 = 15 mg/L) variation versus the corresponding absorbance (A_t/A_0) at 665 nm (inset of Fig. 6A). It is seen that after treatment of the samples in dark for 3 h, RhB concentration in suspension of each sample decreased, a result due to the adsorption of RhB on the sample surface. It has been reported that an appropriate increase in dye adsorption could accelerate its photodegradation [2,33]. The Au/InBi-3D and Pd/InBi-3D samples showed much better RhB degradation activities (C_t/C_0 = 2.4 and 4.5% after 30 min of visible-light illumination, respectively) than the InBi-3D (C_t/C_0 = 6.6%), Ag/InBi-3D (C_t/C_0 = 6.6%), and Pt/InBi-3D (C_t/C_0 = 14.0%) samples. Over the InBi-ref sample, the C_t/C_0 was higher than 8% after 3 h of degradation (inset of Fig. 6A). Such an activity was also inferior to that (7.6% after 150 min of degradation) over the Au/InBi-3D sample for the degradation of RhB aqueous solution (C_0 = 30 mg/L).
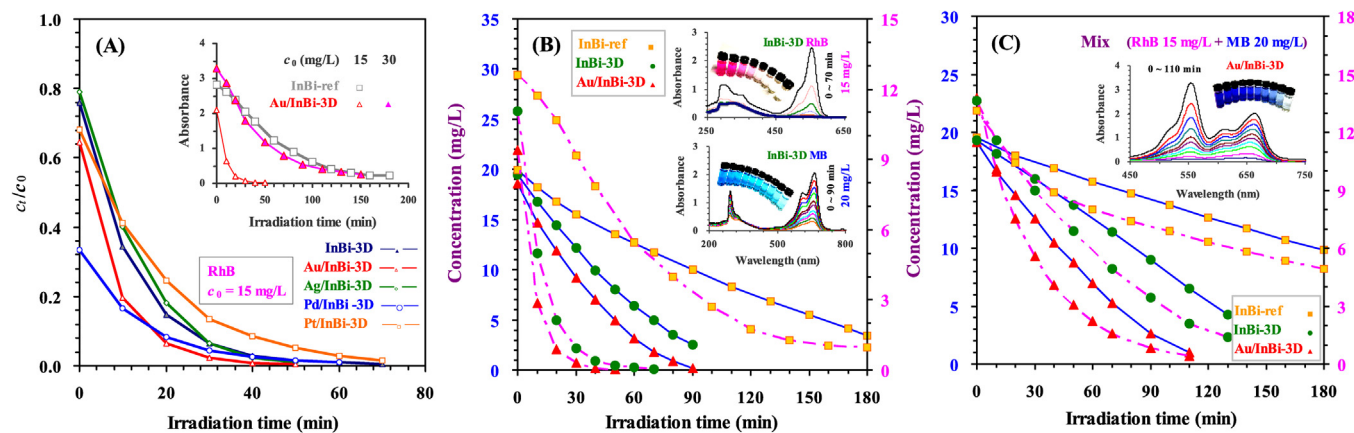
Fig. 6. (A) RhB concentration versus irradiation time for the degradation of RhB aqueous solution ($C_0 = 15$ mg/L) over InBi-3D and M/InBi as well as of RhB aqueous solution ($C_0 = 15$ mg/L) over InBi-ref and of RhB aqueous solution ($C_0 = 15$ and 30 mg/L) over Au/InBi-3D (inset) in the presence of 0.6 mL H_2O_2 under visible-light ($\lambda \geq 400$ nm) irradiation; (B) MB (solid lines) and RhB (dotted lines) concentrations versus irradiation time over InBi-ref, InBi-3D, and Au/InBi-3D for the degradation of MB ($C_0 = 20$ mg/L) and RhB ($C_0 = 15$ mg/L) aqueous solution in the presence of 0.6 mL H_2O_2 under visible-light ($\lambda \geq 400$ nm) irradiation; and (C) RhB (dotted lines) + MB (solid lines) concentration versus irradiation time for the degradation of the RhB + MB aqueous solution over InBi-ref, InBi-3D, and Au/InBi-3D in the presence of 0.6 mL H_2O_2 under visible-light ($\lambda \geq 400$ nm) irradiation. The "Mix" means the RhB + MB mixture.

Therefore, the 3DOM structure was beneficial for the enhancement in photocatalytic activity of the sample. Nevertheless, the InBi-ref sample was more active in degrading RhB than 3DOM InVO$_4$ [21]. This phenomenon might be associated with the synergistic action between InVO$_4$ and BiVO$_4$ of the InBi-based samples. The composites in AgI@TiO$_2$ [2], Ag$_3$VO$_4$/AgBr [7], and Zn$_x$Cd$_{1-x}$S/TiO$_2$ [34] have been claimed to facilitate the separation of photogenerated charges.

The InBi-ref, InBi-3D, and Au/InBi-3D photocatalysts were chosen to measure the activities of MB degradation with an initial MB concentration of 20 mg/L, as shown in Fig. 6B. It is clearly seen that the color of the MB or RhB aqueous solution faded and the absorption bands decreased with irradiation time (inset photos and UV–vis spectra obtained over InBi-3D in Fig. 6B). Apparently, the photocatalytic activity decreased in the order of Au/InBi-3D > InBi-3D > InBi-ref. This result demonstrates the important roles of the plasmonic metal and 3DOM structure. It should be noted that the MB concentration was similar to its initial one ($C_0 = 20$ mg/L) after adsorption on each sample in dark for 3 h. Although the two dyes fellow a pseudo-second-order adsorption kinetic, RhB molecules might be adsorbed mainly on the sample surface while adsorption of MB molecules mainly took place in the mesopores of the sample due to the larger size and steric hindrance of RhB than those of MB [24,35]. It can be seen from Table 3 that there was a difference in performance of bulk InVO$_4$-BiVO$_4$, 3DOM InVO$_4$–BiVO$_4$, and 3DOM Au/InVO$_4$–BiVO$_4$ in the degradation of dyes. For MB degradation, the half-life was about 103.2, 48.5, and 36.4 min over the above three samples, respectively; and for RhB degradation, the half-life was about 40.8, 8.4, and 5.9 min over the above three samples, respectively. It is apparent that the half-life was shorter over the sample with a 3DOM structure, and the loading of plasmonic Au gave rise to a further shorting in half-life. These results indicate that 3DOM structure, noble metal nanoparticles, and composite of InVO$_4$ and BiVO$_4$ played important roles in enhancing the photocatalytic performance of the M/InBi-3D sample. Therefore, the synergistic action of the three factors rendered the 0.08 wt% Au/InBi-3D sample to show the best photocatalytic performance for the degradation of dyes.

To assess the superiority in photocatalytic performance, we carried out the photocatalytic degradation of the MB + RhB mixture (MB and RhB initial concentrations = 20 and 15 mg/L, respectively) over the InBi-ref, InBi-3D, and Au/InBi-3D samples, and the results are shown in Fig. 6C. As expected, the photocatalytic activity of

the Au/InBi-3D sample was much higher than those of the InBi-ref and InBi-3D samples as well as the Degussa P25 sample (Fig. S3C). After 110 min of degradation, the MB and RhB concentrations in the MB + RhB mixture were ca. 1.0 and 0.44 mg/L over Au/InBi-3D, ca. 6.5 and 2.1 mg/L over InBi-3D, ca. 14.1 and 7.2 mg/L over InBi-ref, and ca. 3.5 and 10.4 mg/L over Degussa P25, respectively. Although the MB concentration was lower in the case of Degussa P25, the tile blue color (not shown here) of the final TiO$_2$ powders indicates that MB was possibly adsorbed on the TiO$_2$ surface, which was confirmed by the changes of FT-IR bands at different degradation time (Fig. S4A). We also observed similar phenomena over Au/InBi-3D or InBi-3D (right two photos in Fig. S3C and FT-IR spectra in Fig. S4B and C) when there was no H$_2$O$_2$ in the reaction solutions. It has been reported that the photodegradation extent of the MB + RhB mixture was partially dependent on their own abilities to adsorb on the catalyst surface [24,35]. Compared to the MB + RhB degradation over the Au/InBi-3D sample, MB showed a better adsorptivity on the InBi-3D sample in the dark but a slower degradation after irradiation; no substantial adsorption or degradation of RhB appeared over the two photocatalysts. Taking into consideration of the two blank tests (without a photocatalyst and/or H$_2$O$_2$), one can realize the importance of light and H$_2$O$_2$ in the heterogeneous Fenton reaction [36], because the former could produce e$^-$/h$^+$ pairs [24] and the latter could react with the photogenerated e$^-$ to yield highly reactive hydroxyl radicals that oxidize dye molecules into inorganic products (e.g., CO$_2$, H$_2$O, NO$_3^-$, NH$_3$ or N$_2$) [24,25]. Among all of the as-prepared samples, the 0.08 wt% Au/InBi-3D sample possessed the strongest mineralization ability for MB or RhB. The presence of H$_2$O$_2$ seems to suppress the adsorption of MB on the surface of Au/InBi-3D and InBi-3D in the dark. In other words, H$_2$O$_2$ was apt to adsorb on the positions (micro- or mesopores in the photocatalysts) same as MB, which undoubtedly would facilitate the photocatalytic degradation of MB. Besides of the roles of light and H$_2$O$_2$, the presence of pore structure could improve adsorption of dyes. Therefore, generation of porous structures in a photocatalyst is an efficient way to enhance the photodegradation of dyes (e.g., MB degradation over 3DOM InVO$_4$ with abundant mesopores on the skeletons [20], and RhB degradation over PANI/TiO$_2$ with a unique core-shell mesoporous structure [28]). When the porous materials were modified by transition oxides (e.g., CrO$_x$/3DOM InVO$_4$ [21]), they would become more active photocatalysts for the degradation of RhB. The normalized reciprocal values of the FT-IR relative intensity versus irradiation time over the samples (Fig. S4E) further

Table 3
Reaction orders, correlation coefficients (R^2), rate constants (k), half-life ($t_{1/2}$), and theoretical initial concentrations ($C_{0,T}$), and actual initial concentrations ($C_{0,A}$) for the degradation of MB, RhB, and MB + RhB aqueous solutions in the different photocatalytic systems.

| Sample	MB ($C_t = -kt + C_0$, zero-order reaction)					RhB ($\ln C_t = -kt + \ln C_0$, first-order reaction)				
	R^2	k (mg/(L min))	$t_{1/2}$ (min)	$C_{0,T}$ (mg/L)	$C_{0,A}$ (mg/L)	R^2	k (min^{-1})	$t_{1/2}$ (min)	$C_{0,T}$ (mg/L)	$C_{0,A}$ (mg/L)
0.08 wt% Au/InBi-3D	0.9783	0.2360	36.4	17.17	18.60	0.9992	0.1168	5.9	9.36	9.36
InBi-3D	0.9836	0.1887	48.5	18.31	19.46	0.9990	0.0826	8.4	11.05	11.02
InBi-ref	0.9860	0.0906	103.2	18.70	19.96	0.9927	0.0170	40.8	14.40	12.55
0.08 wt% Au/InBi-3D[a]	0.9915	0.1847	49.7	18.36	19.14	0.9996	0.0313	22.2	14.06	13.72
InBi-3D[a]	0.9996	0.1158	83.7	19.38	19.29	0.9870	0.0172	40.3	14.71	13.56
InBi-ref[a]	0.9960	0.0530	180.3	19.11	19.55	0.9637	0.0050	138.6	11.50	13.08
H$_2$O$_2$[a]	0.9983	0.0318	316.1	20.11	20.05	0.9777	0.0014	495.1	14.24	14.55
Blank[a]	0.9931	0.0139	714.3	19.86	19.95	-	-	-	-	-

[a] For the degradation of RhB + MB aqueous solution.

reveal the discrepancy in absorption and the advantages of good absorption in promoting dye photodegradation [37]. At the same time, one can notice that although the whole time for the mixture degradation was longer than that for the single dye degradation, but it was approximately equal to the total time for the degradation of two dyes. This result suggests that there was a competition mode between the two cationic dyes during photodegradation.

In the degradation of MB or RhB, the zero-order and first-order reaction kinetic models were applied to fit the relationship between the measured dye concentration (C_t) and irradiation time (t): $C_t = -kt + C_0$ and $\ln C_t = -kt + \ln C_0$, in which k refers to the rate constant and C_0 is the initial dye concentration. By considering the correlation coefficients (R^2), one can realize that the degradation of MB over the samples obeyed a zero-order kinetic model (Fig. 7A), whereas the degradation of RhB was a first-order reaction toward RhB concentration (Fig. 7B), similar to the cases reported in the literature [26,28,37]. Table 3 summarizes the kinetic parameters of the samples for the degradation of dyes. Obviously, the rate constants (0.1887 mg/(L min) and 0.0826 min^{-1}) and half-life (48.5 and 8.4 min) over InBi-3D for the degradation of MB and RhB were much higher and shorter than the rate constants (0.0906 mg/(L min) and 0.0170 min^{-1}) and half-life (103.2 and 40.8 min) over InBi-ref, respectively. This result confirms the advantage of the 3DOM structure. When plasmonic Au was decorated on the surface of InBi-3D, the k values increased to 0.2360 mg/(L min) and 0.1168 min^{-1} for MB and RhB degradation, whereas the $t_{1/2}$ values shortened to 36.4 and 5.9 min, respectively. This result indicates the great role of plasmonic metals. The photocatalytic activities of the Au/InBi-3D samples were higher than those of PANI-modified core-shell mesoporous TiO$_2$

microspheres [28], Zn$_x$Cd$_{1-x}$S/TiO$_2$ nanocomposites [34], BiVO$_4$ with a hierarchical heterostructure [37], and A$_2$B$_2$O$_7$ compounds [26]. In the dye mixture degradation over the InBi-ref, InBi-3D, and Au/InBi-3D samples, the k values for either MB or RhB degradation decreased, especially over the first sample the k values decreased to 0.0530 mg/(L min) and 0.0050 min^{-1}, respectively.

3.5. Photocatalytic degradation mechanism

It is well known that a complete photocatalytic process is generally divided into three stages: light harvesting, separation of photogenerated charges, and interfacial reactions [28]. For a high-efficiency photocatalyst, it needs a good implementation at each stage. Based on the above discussion, we propose a photocatalytic mechanism for the degradation of the mixed dyes over the Au/InBi-3D sample, as illustrated in Fig. 8. Due to the different sizes and electronic nature, MB and RhB molecules as well as the H$_2$O$_2$ additive first selectively adsorb in the dark on the specific positions of the periodically porous plasmonic photocatalyst in a competitive mode. Thanks to the excellent optical property of the 3DOM structure and the exceptional surface plasmon resonance of Au nanoparticles well dispersed on the pore walls, a number of high-energy charge carriers (e$^-$/h$^+$ pairs) are photogenerated on the surface of the sample after visible-light irradiation [7]. Then, with the aid of some synergistic effects of Schottky energy barrier and composites in the materials, the photogenerated charge carriers are separated from each other and migrate to different active sites at the semiconductor/liquid or Au/liquid interfaces. The photogenerated e$^-$ can easily react with the dissolved O$_2$ in water to form •O$_2^-$, H$_2$O$_2$ or •OH radicals, while the photogenerated h$^+$
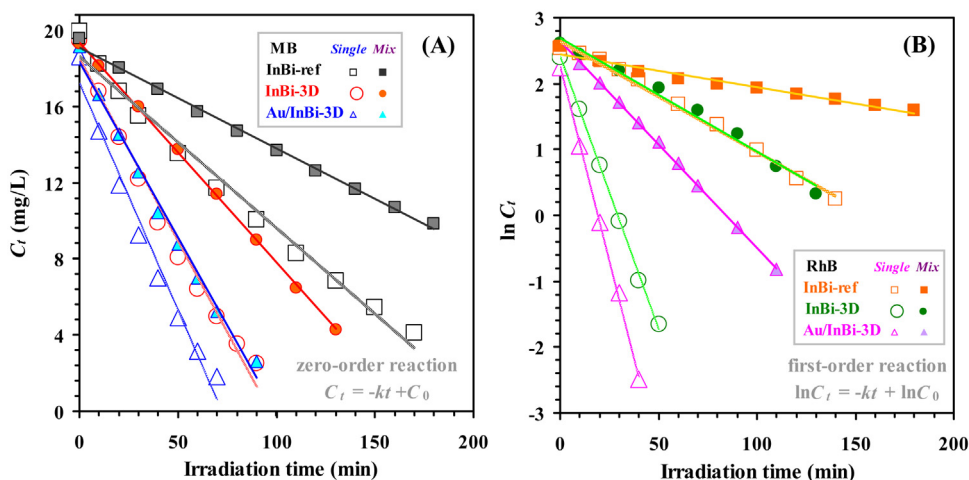
Fig. 7. Kinetic plots for the degradation of MB, RhB, and RhB + MB aqueous solutions by assuming that the degradation takes place over InBi-ref, InBi-3D, and Au/InBi-3D according to (A) zero-order reaction and (B) first-order reaction with respect to MB, RhB or RhB + MB concentration. The "Mix" means the RhB + MB mixture.
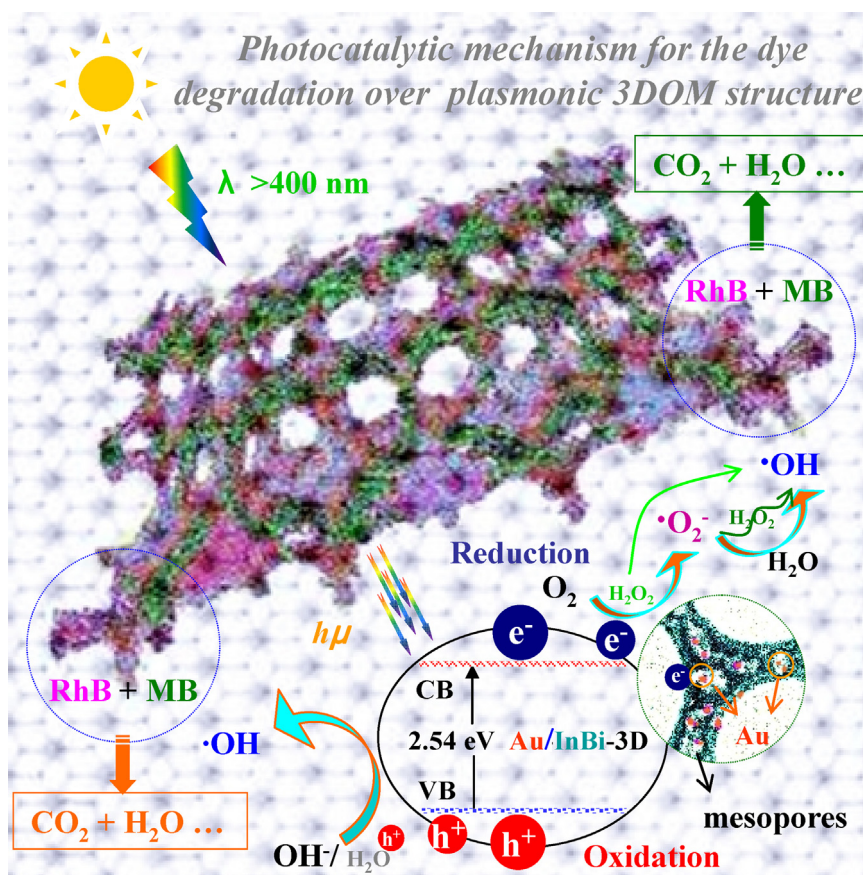
Fig. 8. A schematic illustration of photocatalytic mechanism of dye degradation over Au/InBi-3D in the presence of a small mount of H_2O_2 under visible-light irradiation.

can directly react with OH^- or surface-bound H_2O to form $^\bullet OH$ radicals [3,7,24,38]. It has been reported that the $^\bullet O_2^-$ and $^\bullet OH$ radicals were the uppermost active species in Fenton-like photocatalysis [7,24,38], and a small amount of H_2O_2 in the initial dye solution was beneficial for trapping e^- to form $^\bullet OH$ radicals and also inhibiting the recombination of e^-/h^+ pairs [21,24,36]. The reactive species (e.g., $^\bullet O_2^-$ and $^\bullet OH$ radicals) can persistently attack the dye molecules until they are completely degraded [7,24]. Along with the continuous generation of various electriferous groups, adsorption of the dye molecules on the composite photocatalyst also increased via the electrostatic interactions [35], thus accelerating the interfacial dye degradation.

4. Conclusions

Visible-light-driven InBi-3D and xM/InBi-3D photocatalysts could be prepared via the PMMA-templating and PVA- or PVP-assisted reduction routes, respectively. The as-fabricated samples displayed a surface area of $17–30\,m^2/g$, a M particle size of $2.5–3.8\,nm$, and a bandgap energy of $2.50–2.56\,eV$. The xM/InBi-3D samples performed well in the photocatalytic degradation of MB or RhB: the complete degradation of RhB, MB, and RhB + MB could be achieved within 50, 90, and 120 min over the 0.08 wt% Au/InBi-3D sample, respectively. The degradation of MB and RhB took place according to the zero- and first-order reaction mechanisms, respectively. It is concluded that the 3DOM hierarchical architecture, $InVO_4–BiVO_4$ composite, and high dispersion of plasmonic gold nanoparticles were the main factors responsible for excellent photocatalytic efficiency of the InBi-3D-supported Au sample.

Appendix A. Supplementary data

Supplementary data associated with this article can be found, in the online version, at http://dx.doi.org/10.1016/j.apcatb.2014.10.005.

References

[1] S. Linic, P. Christopher, D.B. Ingram, Nature Materials 10 (2011) 911–921.
[2] C.H. An, W. Jiang, J.Z. Wang, S.T. Wang, Z.H. Ma, Y.P. Li, Dalton Transactions 42 (2013) 8796–8801.
[3] Y. Yan, X.L. Liu, W.Q. Fan, P. Lv, W.D. Shi, Chemical Engineering Journal 200–202 (2012) 310–316.
[4] Y.X. Tang, Z.L. Jiang, G.C. Xing, A.R. Li, P.D. Kanhere, Y.Y. Zhang, T.C. Sum, S.Z. Li, X.D. Chen, Z.L. Dong, Z. Chen, Advanced Functional Materials 23 (2013) 2932–2940.
[5] C.H. An, S. Peng, Y.G. Sun, Advanced Materials 22 (2010) 1–5.

[6] P. Wang, B.B. Huang, X.Y. Qin, X.Y. Zhang, Y. Dai, J.Y. Wei, M.-H. Whangbo, Angewandte Chemie International Edition 47 (2008) 7931–7933.
[7] Q. Zhu, W.-S. Wang, L. Lin, G.-Q. Gao, H.-L. Guo, H. Du, A.W. Xu, The Journal of Physical Chemistry C 117 (2013) 5894–5900.
[8] M. Sadakane, T. Asanuma, J. Kubo, W. Ueda, Chemistry of Materials 17 (2005) 3546–3551.
[9] Y.C. Wei, J. Liu, Z. Zhao, Y.S. Chen, C.M. Xu, A.J. Duan, G.Y. Jiang, H. He, Angewandte Chemie International Edition 50 (2011) 2326–2329.
[10] K.M. Ji, H.X. Dai, J.G. Deng, L.Y. Song, B.Z. Gao, Y. Wang, X.W. Li, Applied Catalysis B: Environmental 129 (2013) 539–548.
[11] M. Sadakane, K. Sasaki, H. Kunioku, B. Ohtani, R. Abe, W. Ueda, Journal of Materials Chemistry 20 (2010) 1811–1818.
[12] H.N. Li, L. Zhang, H.X. Dai, H. He, Inorganic Chemistry 48 (2009) 4421–4434.
[13] Y. Liu, B.C. Liu, Q. Wang, C.Y. Li, W.T. Hu, Y.X. Liu, P. Jing, W.Z. Zhao, J. Zhang, Journal of Catalysis 296 (2012) 65–76.
[14] C.W. Cheng, S.K. Karuturi, L.J. Liu, J.P. Liu, H.X. Li, L.T. Su, A.I.Y. Tok, H.J. Fan, Small 8 (2012) 37–42.
[15] P. Yang, T. Deng, D.Y. Zhao, P.Y. Feng, D. Pine, B.F. Chmelka, G.M. Whitesides, G.D. Stucky, Science 282 (1998) 2244–2246.
[16] J. Du, X.Y. Lai, N.L. Yang, J. Zhai, D. Kisailus, F.B. Su, D. Wang, L. Jiang, ACS Nano 5 (2011) 590–596.
[17] E.S. Kwak, W.M. Lee, N.-G. Park, J.Y. Kim, H.J. Lee, Advanced Functional Materials 19 (2009) 1093–1099.
[18] L.J. Liu, S.K. Karuturi, L.T. Su, A.I.Y. Tok, Energy & Environmental Science 4 (2011) 209–215.
[19] M. Zhou, H.B. Wu, J. Bao, L. Liang, X.W. Lou, Y. Xie, Angewandte Chemie International Edition 52 (2013) 8579–8583.
[20] Y. Wang, H.X. Dai, J.G. Deng, Y.X. Liu, Z.X. Zhao, X.W. Li, H. Arandiyan, Chemical Engineering Journal 226 (2013) 87–94.
[21] Y. Wang, H.X. Dai, J.G. Deng, Y.X. Liu, H. Arandiyan, X.W. Li, B.Z. Gao, S.H. Xie, Solid State Sciences 24 (2013) 62–70.
[22] Y.X. Liu, H.X. Dai, J.G. Deng, L. Zhang, C.T. Au, Nanoscale 4 (2012) 2317–2325.
[23] H.Y. Jiang, H.X. Dai, X. Meng, K.M. Ji, L. Zhang, J.G. Deng, Applied Catalysis B: Environmental 105 (2011) 326–334.
[24] A. Nezamzadeh-Ejhieh, M. Karimi-Shamsabadi., Chemical Engineering Journal 228 (2013) 631–641.
[25] Z. Li, L.W. Mi, W.H. Chen, H.W. Hou, C.T. Liu, H.L. Wang, Z. Zheng, C.Y. Shen, CrystEngComm 14 (2012) 3965–3971.
[26] J.F. Luan, S. Wang, K. Ma, Y.M. Li, B.C. Pan, The Journal of Physical Chemistry C 114 (2010) 9398–9407.
[27] Z.Y. Zhang, I.M. O'Hara, G.A. Kent, W.O.S. Doherty, Industrial Crops and Products 42 (2013) 41–49.
[28] G.Z. Liao, S. Chen, X. Quan, Y.B. Zhang, H.M. Zhao, Applied Catalysis B: Environmental 102 (2011) 126–131.
[29] S.W. Liu, L.S. Zhang, H.L. Xu, W. Zhu, Journal of Molecular Catalysis A: Chemical 252 (2006) 120–124.
[30] J.Q. Yu, Y. Zhang, A. Kudo, Journal of Solid State Chemistry 182 (2009) 223–228.
[31] L.W. Zhang, H.B. Fu, C. Zhang, Y.F. Zhu, Journal of Solid State Chemistry 179 (2006) 804–811.
[32] N. Yamazoe, Y. Teraoka, T. Seiyama, Chemistry Letters 10 (1981) 1767–1770.
[33] X.L. Liang, Y.H. Zhong, H.P. He, P. Yuan, J.X. Zhu, S.Y. Zhu, Z. Jiang, Chemical Engineering Journal 191 (2012) 177–184.
[34] W.J. Li, D.Z. Li, S.G. Meng, W. Chen, X.Z. Fu, Y. Shao, Environmental Science & Technology 45 (2011) 2987–2993.
[35] S. Eftekhari, A. Habibi-Yangjeh, Sh. Sohrabnezhad, Journal of Hazardous Materials 178 (2010) 349–355.
[36] S.J. Yang, H.P. He, D.Q. Wu, D. Chen, X.L. Liang, Z.H. Qin, M.D. Fan, J.X. Zhu, P. Yuan, Applied Catalysis B: Environmental 89 (2009) 527–535.
[37] S. Obregón, G. Colón, Journal of Molecular Catalysis A: Chemical 376 (2013) 40–47.
[38] P.X. Wang, J.J. Xian, J. Chen, Y.H. He, J.X. Wang, W.J. Li, Y. Shao, D.Z. Li, Applied Catalysis B: Environmental 144 (2014) 644–653.